NANO · MICRO small
www.small-journal.com

Antibody Micropatterned Lubricant-Infused Biosensors Enable Sub-Picogram Immunofluorescence Detection of Interleukin 6 in Human Whole Plasma

*Amid Shakeri, Noor Abu Jarad, Jeff Terryberry, Shadman Khan, Ashlyn Leung, Simeng Chen, and Tohid F. Didar**

Recent studies have shown a correlation between elevated interleukin 6 (IL-6) concentrations and the risk of respiratory failure in COVID-19 patients. Therefore, detection of IL-6 at low concentrations permits early diagnosis of worst-case outcome in viral respiratory infections. Here, a versatile biointerface is presented that eliminates nonspecific adhesion and thus enables immunofluorescence detection of IL-6 in whole human plasma or whole human blood during coagulation, down to a limit of detection of 0.5 pg mL^{-1}. The sensitivity of the developed lubricant-infused biosensor for immunofluorescence assays in detecting low molecular weight proteins such as IL-6 is facilitated by i) producing a bioink in which the capture antibody is functionalized by an epoxy-based silane for covalent linkage to the fluorosilanized surface and ii) suppressing nonspecific adhesion by patterning the developed bioink into a lubricant-infused coating. The developed biosensor addresses one of the major challenges for biosensing in complex fluids, namely nonspecific adhesion, therefore paving the way for highly sensitive biosensing in complex fluids.

1. Introduction

Human interleukin-6 (IL-6) is a multifunctional, pro-inflammatory cytokine that has been found to be overexpressed in viral infections, inflammatory conditions and several cancer types such as lung, colorectal, breast, and prostate cancers [1–7] as well as in respiratory infections caused by Severe Acute Respiratory Syndrome Corona Virus 2 (SARS-CoV-2).[8–10] The level of expression in plasma typically reflects severity of the disease, where significantly elevated levels indicate aggressive tumor growth or viral load and poor prognosis in patients.[2,10] Additionally, IL-6 is an important anti-inflammatory cytokine that induces acute responses in chronic inflammatory pathologies. As such, there has been an increasing interest in the use of IL-6 as a biomarker for the diagnosis of early stages of viral infections, cancer, and chronic inflammation.[9–11] A practical IL-6 biosensor should provide a low limit of detection (LOD) (≤5 pg mL^{-1}) and acceptable linear dynamic range (1–100 pg mL^{-1}) in complex fluids, in addition to accuracy, facile operation, and amenable to mass production.[11,12]

There are a large number of different IL-6 detection techniques that have been reported in the literature including electrochemical sensors,[13–22] surface plasmon resonance (SPR),[23–25] chemiluminescence immunoassay (CLIA),[26–29] and immunofluorescence assays (IFA).[30–33] Utilizing 0- and 1-D materials such as carbon nanotubes (CNTs),[14,16] nanoparticles and nanowires,[13,19] as well as porous nanoparticles,[15] optical fibers,[32] and microfluidic platforms,[28] have enabled higher sensitivity in IL-6 detection and to date, electrochemical methods have proven to be the most promising candidate for detection of IL-6 at very low concentrations (0.33 pg mL^{-1} in buffer) with a wide linear dynamic range.[22] While reported IL-6 biosensors have demonstrated satisfactory LODs in buffer or processed serum, their performance in human whole plasma declines significantly, leading to higher LOD's and/or false positive results. In electrochemical sensors, for example, the nonspecific attachment of biological entities in plasma or blood can interfere with the resistivity at the electrodes thereby deteriorating their sensitivity for detection of IL-6 at clinically relevant concentrations.[34] So far, the lowest theoretical LOD for IL-6 detection in plasma was reported by Sabaté del Río et al.[13] This method utilized a complex system composed of 3D BSA nanocomposite, CNTs/Au-nanoparticles, and Au-nanowires and electrochemical detection to obtain an LOD of 23 pg mL^{-1} in human plasma, which exceeds the typical sensitivity requirements of ≤5 pg mL^{-1}.

Omniphobic lubricant-infused surfaces (LISs),[35] have aroused interest as anti-biofouling coatings in recent years due to their ability to repel bacteria, blood cells, proteins, as well as

A. Shakeri, Dr. T. F. Didar
Department of Mechanical Engineering
McMaster University
1280 Main Street West, Hamilton ON L8S 4L7, Canada
E-mail: didar@mcmaster.ca
N. A. Jarad, S. Khan, A. Leung, Dr. T. F. Didar
School of Biomedical Engineering
McMaster University
1280 Main Street West, Hamilton ON L8S 4L8, Canada
J. Terryberry, S. Chen
SQI Diagnostics System Inc
36 Meteor Dr, Toronto ON M9W 1A4, Canada
The ORCID identification number(s) for the author(s) of this article can be found under https://doi.org/10.1002/smll.202003844.

DOI: 10.1002/smll.202003844

their nonwetting properties to different fluids.[36–39] This property is caused by a slippery or low surface tension interface between a monolayer of lubricant, locked into a porous or rough surface and the biofluid or immiscible liquid to be repelled.[40] The omniphobic LIS technology has been employed for antibacterial applications, as well as medical implants and devices where thrombosis and infections could pose a threat;[41–44] however, they have not been implemented as blocking agents for biosensing and we hypothesize that the superior repellency offered by such slippery surfaces may prove to decrease LOD for IL-6 detection in complex fluids.

To verify our hypothesis, we chose an IFA as the sensing platform. IFA's typically fall behind electrochemical sensors in achieving low LOD in buffer and plasma, but they are simple, cost effective and more amenable for point of care diagnostics. Using bead or nanoparticle-based enzyme-linked immunosorbent assay IFA (ELISA-IFA), can enhance the LOD and sensitivity of IFAs for IL-6 detection in buffer, but adds more complexity, and increases the cost.[31–33] Two key aspects that can be modified in ELISA-IFA to further improve its performance and functionality are the proper immobilization of capture biomolecules and the use of optimal surface blocking agents to reduce the background noise often associated with fluorescence-based assays.[45–47] For immobilization of biorecognition elements, contact printing and noncontact printing strategies have been widely used to generate microarrays of biorecognition elements (e.g., antibodies) using desired chemical linkers (e.g., amine or carboxyl groups).[48–50] The microarrays shape, diameter, thickness, homogeneity, and binding mechanism are important attributes to evaluate the efficacy of different microarray biosensing surface strategies.[51] Although several conventional blocking agents are widely used to prevent nonspecific binding, they still result in defects leading to nonspecific attachment and biofouling, and reduce the sensitivity of assays by interfering with immunochemical reactions or specific signal generation.[52,53] Polymers such as Poly(ethylene glycol) (PEG), poly(N-vinylpyrrolidone) (PVP), proteins such as bovine serum albumin (BSA), milk powder, casein, gelatins, sugars such as sucrose, and trehalose and surfactants like Tween 20 are some of the these commonly used blocking agents.[54–56]

In this work, we combined two technologies—microcontact printing of a bioink and lubricant infusion of a fluorosilanized surface—to develop a new biosensing interface for covalently attaching IL-6 capture antibody onto a poly(methyl methacrylate) (PMMA) substrate. To further promote the stabilization of the patterned antibodies through microcontact printing, covalent printing of the capture antibodies was performed via the introduced functional bioinks. Prior to printing onto the surface, the capture antibodies are functionalized via an epoxy-based silane coupling agent that then covalently bind to the free hydroxyl groups on a functionalized surface through the terminal hydroxyl groups of the epoxy-based silane. This provides a robust and stable immobilized capture antibody, that enhances the selectivity and reproducibility of an IL-6 IFA. Applying the LIS anti-fouling coating to the bioink printed PMMA surfaces produced a robust, simple and cost-effective IFA that allowed detection of IL-6 in human whole plasma with an LOD as low as 0.5 pg mL^{-1} and enabled detection in citrated human whole blood during its coagulation induced by calcium chloride. Therefore, the advantages and novelty of our work include: i) Significantly higher sensitivity for detection of IL-6 in complex biofluids such as human whole blood and plasma, ii) Simplicity of the design via using an ELISA based IFA, eliminating any need for use of nanoparticles, nanotubes, nanowires, fibers, and microfluidics. Consequently, the proposed method is low cost and can be mass produced in a short run. iii) Robustness of the device through the covalent immobilization of the capture antibodies onto the FS treated surfaces, and iv) Potential capability for multiplex detection of cytokines via creation of microarrays of different biorecognition elements.

2. Results and Discussion

Antibody embedded lubricant-infused surfaces were created on PMMA, a low-priced polymer with many advantages such as optical transparency, durable chemical and mechanical properties, and recyclability.[57,58] PMMA surfaces were first oxygen plasma treated to induce hydroxyl groups on the surface, and then fluorosilanized via chemical vapor deposition (CVD) of trichloro(1*H*,1*H*,2*H*,2*H*-perfluorooctyl)silane followed by heat treatment at 90 °C to promote the hydrolysis and condensation reactions. Immediately after the plasma treatment, the hydrophilicity of the surface can cause adsorption of water molecules on the surface. During the CVD treatment, the adsorbed water is recruited for oligomerization of trichloro(1*H*,1*H*,2*H*,2*H*-perfluorooctyl)silane prior to its engagement with the plasma induced functional groups. In consequence of the former oligomerization of the trichlorosilane due to the rapid hydrolysis rate of its head groups and the presence of the adsorbed water, stochastically distributed dense self-assembled monolayers (SAMs) of fluorosilane (FS) with an umbrella-shape structure can form across the PMMA substrate (**Figure 1**).[59–64]

Our developed bioink was prepared by serial dilution of (3-Glycidyloxypropyl)trimethoxy-silane (GLYMO) in PBS and mixing the silane solution with the IL-6 capture antibody as explained in Methods. Following the FS treatment of the PMMA, the GLYMO-conjugated bioink was patterned onto the surface via microcontact printing using polydimethylsiloxane (PDMS) stamps (50 × 50 μm^2 arrays of protruded squares). The produced positional microarrays provide improved repeatability of the assay by providing numerous sample replicates inside each well. This plays an important role in the assay performance, as well as its adaptability to high throughput applications. Moreover, since the GLYMO-conjugated capture antibody can covalently bind to the surface, the developed biointerface on the PMMA substrates are very robust. The biofunctional PMMA microarrays were fitted into a superstructure which provides wells for IFA (Figure 1). The wells were subsequently lubricated via perfluoroperhydrophenanthrene (PFPP), a fluorinated lubricant that infuses into the FS SAM and is locked through van der Waals forces on the fluorine groups of FS SAM creating the LIS. This provides the surface with anti-fouling properties against biofluids and proteins thereby diminishing the nonspecific absorption and enhancing the sensitivity of the biosensor. The developed biosensing surfaces were then used for IFA assays for IL-6 detection.

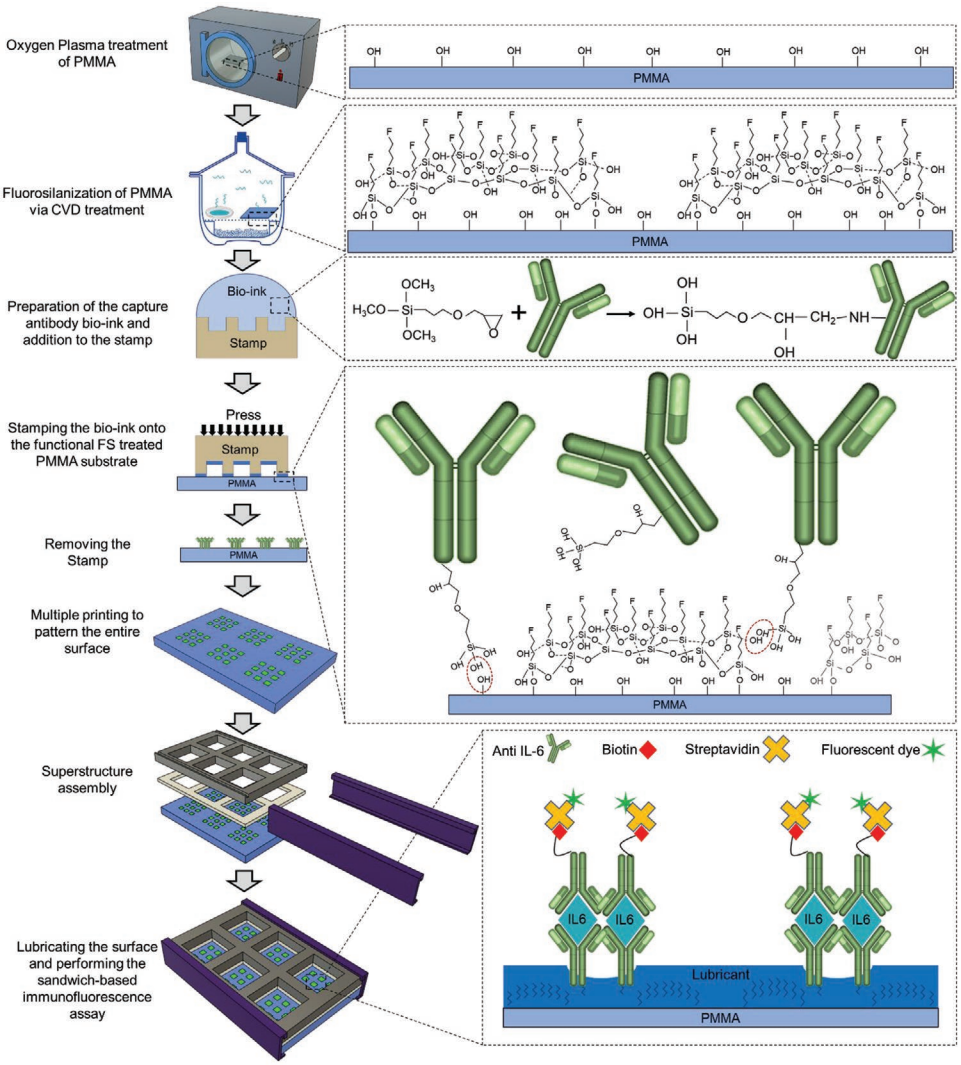

Figure 1. Schematic representation of the process for producing PMMA-based antibody embedded lubricant-infused sensors for IL-6 detection. During the microcontact printing, he IL-6 capture antibody can crosslink to the surface through the reaction between one of the hydroxyls at the head groups of the conjugated epoxy-based silane and the hydroxyl groups remaining after the incomplete FS treatment of the surface (red dash circles).

In order to examine the chemical bonds created after fluorosilanization of PMMA, we conducted high resolution XPS analysis on plain, plasma treated, and FS treated surfaces. **Figure 2** demonstrates deconvoluted spectra of C1s, O1s, and F1s for each sample. The typical deconvolution of PMMA C1s spectra is illustrated in Figure 2a—"plain sample" which consists of a hydrocarbon peak C—C/C—H at 284.57 (±0.1) eV, a beta carbon peak C—C=O at 285.42 (±0.16) eV, C—O bond in methoxy groups at 286.47 (±0.14) eV, and a carboxyl carbon O—C=O peak at 288.58 (±0.2) eV.[65,66] The peak area (%) of C1s components are shown in **Table 1**. As seen, oxygen plasma treatment raised the carboxyl carbon peak area from 12.71% to 18.91%, which could be correlated with oxidation of PMMA and formation of carboxyl groups through plasma induced oxygen radicals.

According to Table 1, the ratio of C-O:O-C = O bonds was also changed from 15.42:12.71 for the plain PMMA surface to 14.67:18.91 for the plasma treated PMMA surface and then down to 6.97:14.19 after the FS treatment. The C-O percentage of plain PMMA shown in the Cs1 spectra could be due to the methyl groups of PMMA. During plasma treatment, these methyl groups on PMMA (highlighted with a circle in Figure S1 in the Supporting Information) are partially reduced. At the same time, plasma induced C-OH groups can be created on the surface. Thus, the resulting effect is minimal change in the abundance of C-O groups before and after plasma treatment. Simultaneously, plasma treatment can increase the amount of carboxyl groups on the surface as discussed previously. As a result, there is a slight shift in the C-O:O-C = O ratio toward O-C = O bonds. During the fluorosilanization of the surface, the broken C-O groups can be replaced by FS groups. Moreover, the heat treatment step conducted after FS treatment can result in partial hydrophobic recovery of the PMMA surface. Thus, hydroxylated PMMA can lose its hydrophilic C-OH and O-C = OH groups induced by the initial plasma treatment. This could be the reason for slight reduction of O-C = OH groups

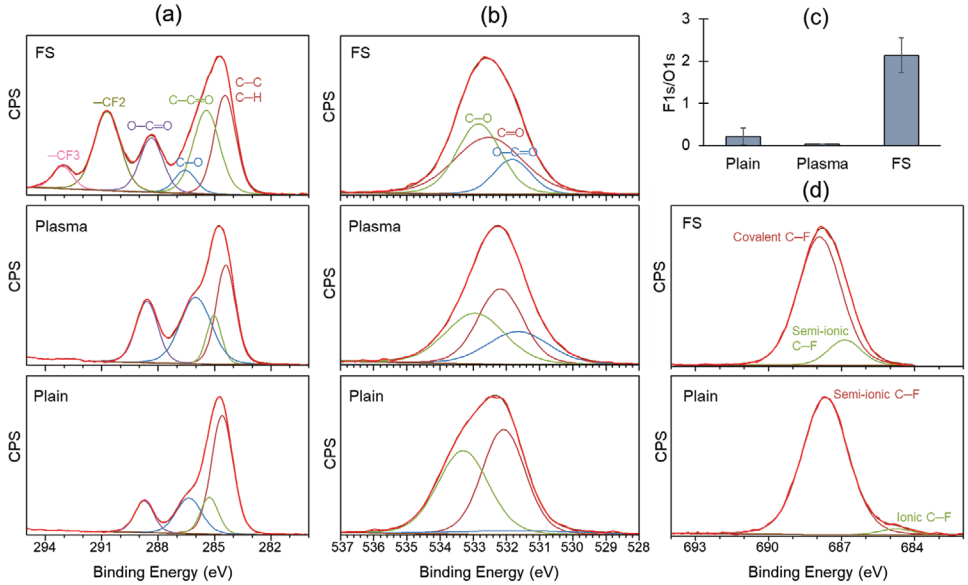

Figure 2. Deconvoluted high resolution XPS spectra of a) C1s, b) O1s, and d) F1s, for the PMMA surface before plasma treatment (plain), after the plasma treatment (plasma), and after fluorosilanization (FS). c) F1s/O1s peak area ratio before and after PMMA surface modification. Data are shown as mean ± SD.

after FS treatment. However, regarding C-O groups, there is relatively more reduction in the area percentage of C-O groups even compared to the plain PMMA surface due to the hydrophobic recovery of the plasma induced C-O groups as well as the replacement of the methyl groups of PMMA by FS groups during the silanization.

Although fluorosilanization of PMMA surfaces reduced the percentage of carboxyl groups to 14.19%, there was an increase in carboxylic groups compared to the control. The remaining carboxylic groups with functional OH moieties on the surface could be as a result of short CVD and heat treatment durations we employed in this study (i.e., 30 min for each step) which led to incomplete polymerization of FS SAMs. Furthermore, the incomplete polymerization can provide functional hydroxyl groups at the umbrella-shape SAMs. The unreacted silanol groups at FS SAMs could also be a consequence of the reasonable values of bond lengths and angles that silanol bonds can only take.[67,68] The remaining hydroxyl groups provide functionality for further immobilization of anti-IL6 antibody bioink. In fact, at higher CVD durations, we were unable to properly microcontact print the capture antibody onto the treated PMMA surfaces which could be attributed to lack of OH groups on the surface.

In microcontact printing, the IL-6 capture antibody can physically attach to the hydrophobic surface via hydrophobic interactions. By conjugating the capture antibody with GLYMO, covalent attachment of the antibody increases, leading to a higher yield of antibody immobilization. As illustrated in Figure 1, the epoxy moiety at the tail group of GLYMO could first couple with the primary and secondary amines of the antibody throughout the bioink formation. During the microcontact printing, we hypothesized the possibility for any of the OH head groups of epoxy silane in the bioink to randomly react with the OH groups of FS SAMs remained after the incomplete fluorosilanization of the surface. For instance, in the umbrella structure of FS, the hydrolyzed head groups of GLYMO can react with the OH groups tethering on the sides of the FS umbrella causing small buckling/bending of siloxanes. Moreover, given the fact that the surface is not fully covered with FS umbrella SAMs, The trifunctional GLYMO can bind to the remaining OH groups located potentially between the areas covered by FS SAMs (Figure 1), creating C–O–Si bonds. In Figure 1, the schematic related to the covalent attachment of GLYMO-conjugated antibodies exhibits potential reactions that can happen between the OH groups of GLYMO and the FS treated surface.

In Figure 2a, fluorosilanization of PMMA resulted in the appearance of two new peaks in the C1s spectrum at 290.69 and

Table 1. Quantification of the peak area percentages of C1s spectra for PMMA surfaces before and after the surface modification. Data are shown as mean ± SD.

Binding energy [eV]	284.57 (±0.1)	285.42 (±0.16)	286.47 (±0.14)	288.58 (±0.2)	290.69 (±0.06)	293.05 (±0.06)
Chemical bond	C–C/C–H	C–C=O	C–O	O–C=O	–CF2	–CF3
			Peak area [%]			
Plain PMMA	56.41 (±1.18)	14.45 (±2.73)	15.42 (±2.83)	12.71 (±0.45)	0	0
Plasma treatment	49.83 (±5.96)	16.59 (±2.52)	14.67 (±4.71)	18.91 (±3.3)	0	0
FS treatment	23.58 (±1.06)	23.48 (±4.3)	6.97 (±1.62)	14.19 (±0.98)	26.25 (±3.44)	5.52 (±0.64)

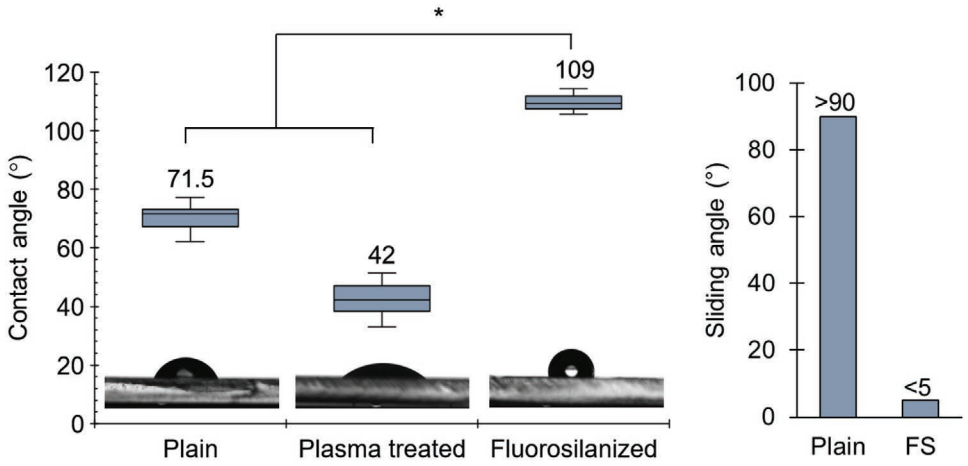

Figure 3. Contact angle and sliding angle results of PMMA surfaces before and after the surface modification. Error bars represent the standard deviation. There is a significant difference in the contact angles with $*P \ll 10^{-7}$.

293.05 eV which are associated with −CF2 and −CF3, respectively.[69,70] These peaks confirm the formation of FS layer with the linear formula of $CF_3(CF_2)_5CH_2CH_2SiCl_3$ as the precursor. The O1s spectrum of plain PMMA surface in Figure 2b can be deconvoluted into primarily two peaks of C−O at ≈533.3 eV and C=O at 532 eV.[71–73] Plasma treatment of the surface advanced a peak at ≈531.6 eV attributed to O−C=O bond [74] which remained in the O1s spectrum after fluorosilanization of the surface, indicating the presence of functional OH groups on the FS treated PMMA surfaces. The peak area ratio of F1s/O1s is plotted in Figure 2c which reveals a substantial increase in the amount of fluorine atoms on PMMA surfaces through the FS treatment. The F1s spectra of plain PMMA surface (Figure 2d) consisted of semi-ionic C−F bond at ≈687.5 eV, as well as ionic C−F bond at ≈684.5 eV.[75] These bonds were completely etched and removed via oxygen plasma treatment of the surface. Fluorosilanization of the PMMA surface resulted in the emergence of covalent C−F bond at ≈688 eV [76] which depicts the robust FS SAM created onto the PMMA substrate. Notably, we performed the XPS test a month after the surface functionalization to confirm the stability of the functional groups onto the PMMA surfaces.

The omniphobic properties of the fluorosilanized PMMA surfaces were quantified using contact angle and sliding angle measurements (**Figure 3**). The contact angle and sliding angle of plain PMMA surfaces before any treatment were estimated at 71.5° and >90°, respectively. After 15 min of oxygen plasma treatment, the contact angle dropped to 42° due to formation of hydroxyl groups. Fluorosilanization of the PMMA surfaces for half an hour via CVD technique significantly increased the contact angle to 109°. It is worth mentioning that higher surface hydrophobicity and contact angles can hinder printing the antibodies through microcontact printing protocol with PDMS stamps. Measuring the angular slip of the LIS estimated its interfacial tension and omniphobicity.[77,78] For this purpose, PFPP lubricant was added to the surface and the excess amount of lubricant was removed by tilting the substrate. Infusing the lubricant into the surface can change the surface energy of the substrate and create a slippery interface on which water-based solutions and biofluids can easily slide off by a tremble. The thin layer of the lubricant trapped onto the FS treated surfaces reduced the sliding angle to less than 5°. When the lubricant was added to a plain PMMA surface, due to the absence of FS groups, the lubricant completely came off the surface after tilting the substrate, resulting in no slippery properties. Notably, printing of the antibodies did not significantly impact the average contact angle and hydrophobicity of the PMMA surfaces as the antibody arrays occupy only a small portion of the substrate. However, due to the fact that droplets can be pinned at the printed areas, which is desirable considering the applicability of the surface for IFA, the sliding angle of the surface changed after patterning, and the droplets could not slide off the entire PMMA surface. The high contact angle and low angular slip of the FS treated PMMA surfaces indicate repellent behavior of the surfaces against different proteins and biomolecules in solution, a key characteristic to prevent nonspecific adhesion for biosensing. It should be mentioned that after even 5 min of FS CVD treatment of the PMMA surfaces, we were still able to get high contact angles comparable to the 30-min CVD treatment time due to the rapid formation of nano-sized FS SAMs on the surface. However, the samples that were treated for shorter CVD times did not exhibit proper sliding properties which could be because of the inadequate FS groups on the PMMA surface for locking a sufficient amount of lubricant on the surface.

In order to confirm the robust attachment of the IL-6 capture antibody onto the FS treated surfaces, we microcontact printed fluorescently labeled BSA-FITC conjugated with GLYMO and compared the results with unconjugated BSA-FITC sample as a control. As shown in Figure S2 in the Supporting Information, conjugating BSA-FITC with GLYMO before printing can bring about a higher yield of BSA-FITC patterned on the surface. This shows the positive effect of epoxy conjugation on the efficacy of the printed proteins via microcontact printing. Moreover, in order to show the printed proteins do not wash off throughout the washing steps in the assay, we submerged the samples in the buffer of tris-buffered saline mixed with Tween 20 (TBST) which we used in the IL-6 detection assay. In addition, we shook the samples at 100 RPM inside the buffer for 24 h. After imaging the samples, we noticed that there was no

significant difference in the fluorescence intensity of the patterns achieved via BSA-FITC conjugated with GLYMO, while in the control sample, the patterns were almost completely washed off (Figure S2, Supporting Information).

To detect IL-6 using IFA, recombinant IL-6 present in either buffer or plasma was added to the antibody printed lubricant-infused PMMA sensors at various concentrations ranging from 0 to 2500 pg mL^{-1}. Since the unprocessed human whole plasma contains several interfering biological entities such as clotting factors, hormones, albumins, and fibrinogen, detection of IL-6 in such a complex biofluids can attest to the enhanced sensitivity of the biosensor. The sandwich assay was followed by addition of a biotinylated IL-6 detector antibody and a fluorescently labeled streptavidin (**Figure 4**a,b). Representative images of the detection fluorescent arrays at different IL-6 concentrations in buffer and plasma are shown in Figures S3 and S4 in the Supporting Information, indicating the microarrays of IL-6 are clearly distinguishable in both plasma and buffer at the concentration of 0.5 pg mL^{-1}. FiJi ImageJ software [79] was utilized to process and quantify the mean fluorescent intensity (MFI) of each printed square. As a confirmatory method to FiJi Image J, Chan-Vese segmentation[80,81] image processing in Python was performed for quantification of results in buffer. Figure 4c,d, illustrates representative fluorescence images of the microarrays of IL-6 at a concentration of 312.5 pg mL^{-1} before and after the Chan-Vese segmentation. Results of Chan-Vese segmentation processing on the other sample concentrations can be seen in Figure S5 in the Supporting Information.

Table 2 illustrates the results of the IL-6 IFA in both buffer and plasma. Two separate and individually processed imaging methods were used to confirm equivalent MFI results in buffer. The more sophisticated Chan-Vase Python approach reduces the influence of artifacts and outliers. The error values corresponding to each result is indicated as coefficient of variation (CV%) in Table 2. The LIS IL-6 IFA yielded a functional LOD of 0.5 pg mL^{-1} which was significantly differentiated ($p < 5 \times 10^{-6}$) from the 0 pg mL^{-1} control for both raw and background-subtracted MFI values in buffer and plasma (Tables S1 and S2, Supporting Information).

Figure 4e shows the linear dynamic range of MFI as a function of concentration. The linear range obtained form LIS IL-6 IFA after standard curve fitting was 0.5–156 pg mL^{-1} with the $R^2 > 0.97$. This dynamic range includes the required LOD sensitivities for oncological applications such as leukemia (1.45 pg mL^{-1} [82]) breast cancer (3–50 pg mL^{-1} [83]), prostate cancer (4–7 pg mL^{-1} [84,85]), ovarian cancer (10 pg mL^{-1} [86]), and liver cancer (12 pg mL^{-1} [2]). Importantly, the current dynamic range is also applicable for detection of Covid-19 (SARS-Cov2) infection (5.8–64 pg mL^{-1} [10]). Both buffer and plasma were also plotted with a quadratic (third degree polynomial) curve fit for the dynamic range of the LIS IL-6 IFA of 1–312.5 pg mL^{-1} shown in Figure S6 in the Supporting Information. IL-6 detection results in plasma and buffer demonstrated almost similar MFIs, indicating that the developed biosensor is capable of preventing nonspecific binding and interference in plasma enabling detection of low concentrations of IL-6 in plasma. In

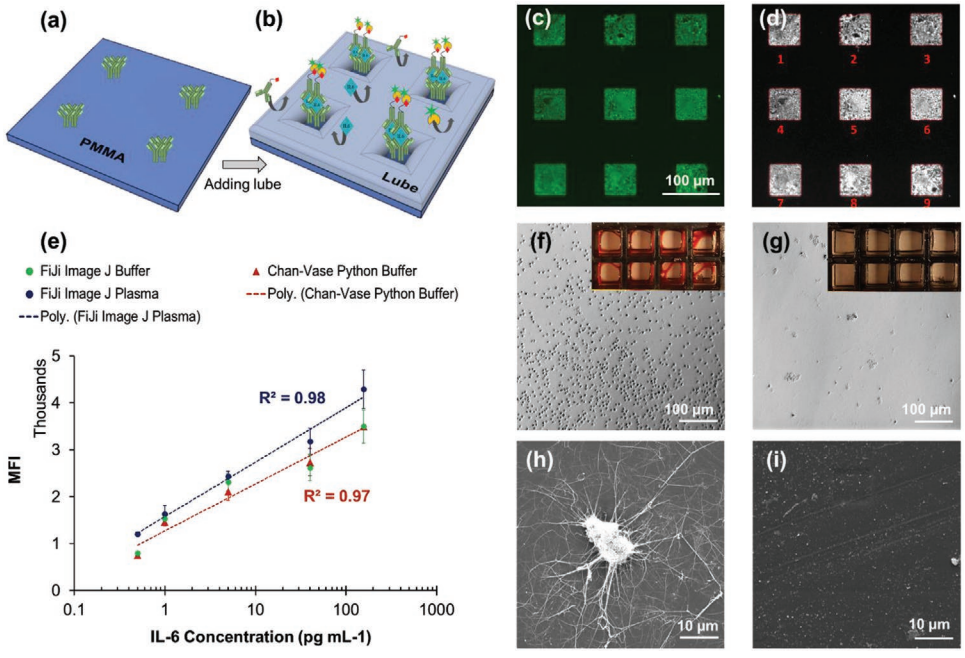

Figure 4. a) Schematic representation of FS treated PMMA surface patterned with the capture antibodies. b) Schematic representation of FS treated PMMA surface after adding the lubricant and performing the IFA. The lubricant layer repels all sorts of biofluids and proteins while capturing the target at the printed areas. c) Raw image of the IL-6 microarrays at the concentration of 312.5 pg mL^{-1} in buffer. d) Image (c) after the Chan-Vese image segmentation processing in Python. e) Linear dynamic range of dose response curves of the IL-6 IFA using LIS. Graphical data are shown as mean ($n = 18$ replicates, $R^2 \geq 0.97$ for buffer and ≥0.98 for plasma) with linear range of 0.5–156 pg mL^{-1}. Error bars represent the ± standard deviation. f,g) Optical microscope images of the blood cells attached to the untreated (plain) PMMA and LIS PMMA, respectively, following whole blood coagulation test. The inset images show the wells after the clotting assay. The area of each well is ≈1cm^2. h) SEM image of the blood clot attached to the plain PMMA surface. i) SEM image of antibody-printed LIS PMMA surface after the clotting assay.

Table 2. Standard curve MFI values and precision for the LIS IL-6 IFA in buffer and plasma using two image processing methods.

Concentration pg/mL	Buffer					Plasma	
	Background Subtracted MFI FiJi ImageJ	%CV Raw FiJi ImageJ	Background Subtracted MFI Chan-Vese Python	%CV Raw Chan-Vese Python	% Robust CV Background Subtracted Chan-Vese Python	Background Subtracted MFI FiJi ImageJ	%CV Raw FiJi ImageJ
2500	12 278	14.0	12 658	13.6	17.1	9576	15.0
312.5	8156	10.9	7938	10.9	23.8	5523	7.4
156	3499	10.1	3495	10.2	17.0	4291	9.5
40	2622	10.7	2737	10.8	31.2	3184	8.7
5	2310	8.1	2107	8.7	28.6	2439	4.4
1	1538	5.3	1465	5.7	32.2	1634	11.3
0.5	804	2.3	755	2.6	25.2	1207	3.5
0	150	1.4	19	1.3	N/A	338	3.0

Table S3 in the Supporting Information, the superior performance of the presented biosensor for IL-6 detection in human plasma is compared to the recent most well-known techniques along with their associated advantages and disadvantages. It is worth mentioning that the antibody-antigen interactions used as a based mechanism to capture IL-6 in this work, is intrinsically specific and it has been shown that there is not any nonspecific interaction between the anti-IL-6 monoclonal antibody and other types of cytokine such as IL-2, IL-3, IL-4, IL-5, IL-8, IL-9, IL-11, TNF-α, TNF-β, IFN-α, and IFN-γ.[33] Consequently, the specificity of our developed biosensor is adequately high for multiplex detection of cytokines.

In order to evaluate the performance of the developed biosensing surface in human whole blood, we examined the capability of the assay to recover IL-6 spiked into recalcified citrated blood. The calcified blood was spiked with IL-6 at the concentration of 312.5 pg mL^{-1} and incubated on the LIS sensing interface for an hour during blood coagulation process. Recovery of the spiked sample (n = 9 replicates) on the plasma standard curve was 119.4% which is within the accuracy acceptance criteria of ± 20% bias. This corresponds the upper limit of quantitation of the LIS IL-6 IFA and indicates that the assay is able to detect IL-6 in whole blood (Figure S7, Supporting Information). We believe that this is the first report on performing biosensing in activated human whole blood while it coagulates.

In addition, a blood adhesion assay was conducted to evaluate the repellency of the surface treatment against fibrin-induced blood clot to the developed PMMA biosensing substrates. Figure 4f depicts a representative optical microscope image of blood cells attached onto the plain PMMA surface, following clot formation after an hour of incubation with recalcified citrated blood. The substrates were washed three times with tris buffered saline (TBS) and TBS Tween 20 (TBST) before imaging. The inset image in Figure 4f reveals the formed blood clots remaining on the plain PMMA surfaces after the washing steps. However, LIS coating significantly suppressed blood clot attachment to the surface (Figure 4g). Owing to the omniphobic characteristic of the treated PMMA surface, the clot that was formed during the blood incubation could readily be washed off the surface by the wash buffers used in the assay, while in the case of untreated PMMA surfaces, the clot remained stable onto the surface throughout the washing steps. Figure 4h,i shows the SEM images of the untreated PMMA surface compared to antibody embedded LIS after fixation of the remaining clot and fibrins.

Therefore, the antibody embedded lubricant-infused PMMA biosensor not only prevents nonspecific adhesion of blood cells, but also enables IL-6 detection during the clot formation, facilitating accurate detection in nonanticoagulated whole blood, which could enable future *ex-vivo* and in vivo biosensing platforms as well as biosensing in blood-contacting wearable devices.[87]

3. Conclusion

A unique biosensing interface was presented that enables sub picogram detection of IL-6 in human plasma as well as in coagulating human whole blood. This was achieved by printing the developed bioink solution into a fluorosilanized PMMA substrate followed by infusion of a thin lubricant layer. The presented biosensing interface benefits from the repellency and omniphobicity of the LIS, which blocks nonspecific attachment of interfering matrix components to the surface, thereby enhancing the sensitivity and specificity of the biosensor. Another factor contributing to the achieved low LOD, is the bioink, composed of epoxy-based silane-anti-IL-6 complexes, enabling covalent microcontact printing of the capture antibody onto the FS PMMA surface. The developed biointerfaces promote covalent binding to the FS surface with various biomolecules through their amine moieties using this new bioink preparation technique. The presence of epoxy as a cross-linking agent in the bioink facilitates the transfer of the antibodies from the PDMS stamps to the FS treated PMMA substrate, leading to a higher yield of antibody patterned onto the surface.

The presented fabrication method is simple and scalable for mass production and can be applied to different substrates and for the detection of other disease markers. An important advantage of the developed biosensor is that since the substrate is covalently coated with a monolayer of fluorosilane, the repellency behavior of the surface is much more durable in comparison to common blocking agents that are physically or electrostatically attached to the surface. Furthermore, as we are able to covalently micro pattern the FS surface with the desired capture antibody, the stability of the immobilized biomolecules is significantly increased. Future efforts will focus on design

and optimization of a process for mass production of the developed biosensing interfaces as well as enabling multiplex detection of target biomarkers.

4. Experimental Section

Materials: The following materials and reagents have been utilized for surface biofunctionalization and IL-6 sandwich immunoassay: trichloro(1*H*,1*H*,2*H*,2*H*-perfluorooctyl)silane (TPFS) (Sigma-Aldrich, Oakville, ON, Canada), (3-glycidyloxypropyl)trimethoxy-silane (GLYMO) (Sigma-Aldrich, Oakville, ON, Canada), perfluoroperhydrophenanthrene (PFPP) (Sigma-Aldrich, Oakville, ON, Canada), polydimethylsiloxane (PDMS) (Dow SYLGARD 184 Silicone Encapsulant, Ellsworth Adhesives, Stoney Creek, ON, Canada), albumin–fluorescein isothiocyanate conjugate (BSA-FITC) (Sigma-Aldrich, Oakville, ON, Canada), recombinant human (*E. Coli* derived) IL-6 (R&D Systems, Minnesota, US), IL-6 monoclonal antibody (MQ2-13A5, capture antibody) (ThermoFisher Scientific, ON, Canada), biotinylated IL-6 monoclonal antibody (MQ2-39C3, detector antibody) (ThermoFisher Scientific, ON, Canada), BV480 streptavidin (BD Horizon™, Mississauga, ON, Canada), and Poly(methyl methacrylate) plates (PMMA) (Beauty Glass, Hsin Hwa Chemical Co, Ltd, Taiwan). Human blood plasma, and citrated whole human blood were used as received without any modification and collected from healthy donors who provided a signed consent for collecting their blood. The procedure was approved by the McMaster University Research Ethics Board.

Surface Fluorosilanization: Before functionalization of PMMA, the substrates were cut to the size of a glass slide (75 mm x 25 mm), and carefully washed using water and ethanol to remove any traces of impurities. The PMMA surface was initially oxygen plasma treated for 15 min (Harrick Plasma) to hydroxylate the surface. Afterward, the substrate was immediately transferred to a vacuum desiccator in order to perform fluorosilanization through CVD method using trichloro(1*H*,1*H*,2*H*,2*H*-perfluorooctyl)silane for 30 min at –0.08 MPa pressure. Subsequently, the fluorinated surface was placed on a hot plate at 90 °C for 30 min to create FS SAM (Figure 1).

Preparation and Microcontact Printing of the Bioink: (3-glycidyloxypropyl)trimethoxy-silane was diluted in PBS to achieve the concentration of 22.4×10^{-6} M. Then, IL-6 monoclonal capture antibody was mixed with the epoxy solution at the concentration of 150 μg mL^{-1}. The prepared bioink was patterned on the fluorosilanized PMMA surface through microcontact printing. In order to make PDMS stamps, a silicon wafer mold with the desired patterns was fabricated using photolithography technique. PDMS was cast into a mold to produce stamps with an array of square protrusions (50×50 μm^2). The stamps were sonicated in ethanol and dried before use. The required amount of the capture antibody bioink (≈5 μL) was added to each stamp to cover the entire features of the stamps and incubated for 10 min. Thereafter, the stamps were washed with PBS and then water and dried for a 2–4 s using a strong blast of compressed air. The stamps were immediately pressed onto the FS treated PMMA surface by placing a small amount of weight on top. After 2 min, the stamps were removed, and the surfaces were incubated in a humidified atmosphere at 4 °C for around 1 h and a half. To conjugate BSA-FITC with (3-glycidyloxypropyl)trimethoxy-silane, 100 mg mL^{-1} of BSA-FITC (diluted in PBS) was mixed with GLYMO at the same ratio as for the IL-6 capture antibody.

Lubricant Infusion of the Fluorosilanized Surface: Following the covalent antibody printing onto the fluorosilanized surface and assembly of the superstructure (Figure 1), PFPP lubricant was added to the wells and incubated for about 1–2 min. Then, the surface was flipped to remove the excess amount of the lubricant and washed with Tris buffered saline (TBS) and TBS Tween 20 (TBST) leaving a thin layer of lubricant trapped within the fluorine groups of the surface.

Surface Characterization: High-resolution X-ray photoelectron spectroscopy (XPS) (PHI Quantera II, Biointerfaces Institute, McMaster University) was implemented to reveal the chemical bonds which appeared on the surface before and after the plasma treatment and after the fluorosilanization step. Worth mentioning that we decided to perform XPS 1 week after the surface treatment to ensure the chemicals and functional groups of the modified surfaces remain stable. C1s, O1s, and F1s peaks were recorded in the high resolution XPS analysis and the raw data was deconvoluted incorporating CasaXPS application.

The hydrophobicity and surface tension of the PMMA substrates were quantified using contact angle and sliding angle techniques. The contact angles of plain, oxygen plasma treated, and fluorosilanized PMMA surfaces were measured via Future Digital Scientific OCA20 goniometer (Garden City, NY). In these experiments, 2 μL of deionized water was dropped onto the multiple spots of the surfaces and the contact angles were automatically calculated from the captured images of the droplets. A digital angle level (ROK, Exeter, UK) was adopted to measure the sliding angles of the plain and fluorosilanized PMMA samples. Before adding 2 μL of deionized water to the surfaces and obtaining the sliding angles, both plain and FS treated surfaces were lubricated with the PFPP lubricant and tilted to remove the excess amount of the lubricant. The droplets were placed onto the substrates at various angles, and the angle at which the droplet starts sliding off the surface was assigned as the sliding angle.

IL-6 Immunofluorescence Assay (IFA): Recombinant IL-6 solution was serially diluted in either sample diluent composed of 1% BSA in phosphate-buffered saline (PBS) or human blood plasma to produce the different concentrations of 2500, 312.5, 156, 40, 20, 5, 2, 1, 0.8, and 0.5 pg mL^{-1}. 150 μL of the IL-6 solution was added to each well and incubated for an hour. Next, the wells were washed again using TBS and TBST, and biotinylated IL-6 monoclonal antibody (1:500 v:v diluted in the sample diluent buffer) was added to the wells and incubated for anhour. Finally, the wells were washed using both wash buffers, and the BV480 streptavidin dye (1:250 v:v diluted in the reporter buffer) was added to each well and incubated for 30 min in complete darkness. The well plate was washed with the wash buffers before the imaging.

Fluorescence Microscopy: Fluorescent imaging was conducted via a Zeiss inverted fluorescent microscope (AX10) using Fluorescein (FITC) filter set. The images were acquired via ZEN software under 10X magnification. In FiJi ImageJ software, the acquired 16-bit TIF images were first divided into individual colors (Image Color Split Channels). Next the Image Adjust Threshold function was used to define a printed square's positive signal. Square command was used to enclose a square around the PDMS stamped region. The pattern of squares for each well is replicated between images with the Take command of the ROI Manager. The median MFI signal intensities were then obtained by using the Measure command. Four smaller squares were then overlaid on the blank regions between the printed squares to obtain the background signal which was then subtracted from the MFI of the patterned areas for each well. The resulting raw data is processed by averaging the 9 positive and 4 negative spots for each image. Duplicates of each sample, control or standard yielding 18 replicate squares for each measurement were evaluated on the IL-6 IFA PMMA slides,

In Chan-Vese segmentation image processing in Python, pixels within the red border demark the spot region while pixels outside the red border belong to local background. Spot signal is calculated as the MFI of spot region minus the median pixel value of local background (i.e., background subtraction). For each level, a "raw" mean and standard deviation are calculated from the signals of 18 replicates. In addition, Tukey Biweight algorithm has been applied on the raw data to obtain the robust mean and standard deviation (i.e., weighted mean & STD) in order to minimize the influence of outliers.

The two-tailed student T-test assuming unequal variance was used for analysis of significant differences between IL-6 levels of the dose response curve. The fitting trendlines in the dose respond graph was done by a logarithmic relationship of Equation (1)

$$MFI = a \times \ln(x) + b \tag{1}$$

where x is the IL-6 concentration in pg mL^{-1}, and a and b are the fitting parameters. The number of tests for each concentration was 3.

Blood Clot Formation and Scanning Electron Microscopy (SEM) Imaging: By initiating blood clot formation onto PMMA substrates, we assessed the blood cells and proteins interactions with our modified lubricant-infused surfaces compared to untreated PMMA surfaces. In order to initiate the clot, 100 µL of the citrated human blood was recalcified by 100 µL of 25×10^{-3} M $CaCl_2$ (diluted in HEPES) and added to each of the wells with the treated and untreated PMMA bottom surfaces. After 1 h incubation, the clot was gently removed, and the wells were washed several times with TBS and TBST wash buffers. Further, 2% glutaraldehyde (diluted in PBS) was added to the wells and incubated overnight to fix the clot. After proper washing, the surfaces were incubated for 1 h with 1% osmium tetroxide in 0.1 M sodium cacodylate buffer to proceed with the post-fixation. The surfaces were dehydrated through a graded series of ethanol, and then critical point drying was performed on the samples by Leica EM CPD300 dryer (Leica Mikrosysteme GmbH, Wien, Austria) using liquid CO_2 flush. The samples were then sputtered with gold (Polaron Model E5100 sputter coater, Watford, Hertfordshire) and imaged via SEM (JSM-7000 F).

Supporting Information

Supporting Information is available from the Wiley Online Library or from the author.

Acknowledgements

The authors acknowledge and thank Professor Zeinab Hosseinidoust for critically editing the paper. This work was supported by NSERC Discovery and CRD grants, Ontario Early Researcher Award grant, and McMaster start-up funds to T.F.D.

Conflict of Interest

The authors declare no conflict of interest.

Keywords

bioinks, biosensing in plasma, immunofluorescence assays, interleukin 6 detection, lubricant-infused surfaces

Received: June 24, 2020
Revised: August 23, 2020
Published online:

[1] S. Grivennikov, M. Karin, *Cancer Cell* **2008**, *13*, 7.
[2] Y.-C. Chung, Y.-F. Chang, *J. Surg. Oncol.* **2003**, *83*, 222.
[3] Z. Culig, M. Puhr, *Mol. Cell. Endocrinol.* **2012**, *360*, 52.
[4] C. Dethlefsen, G. Højfeldt, *Breast Cancer Res. Treat.* **2013**, *138*, 657.
[5] H. Yanagawa, S. Sone, Y. Takahashi, T. Haku, S. Yano, T. Shinohara, T. Ogura, *Br. J. Cancer* **1995**, *71*, 1095.
[6] M. Lesina, M. U. Kurkowski, K. Ludes, S. Rose-john, M. Treiber, G. Kloppel, A. Yoshimura, W. Reindl, B. Sipos, S. Akira, R. M. Schmid, H. Algul, *Cancer Cell* **2011**, *19*, 456.
[7] N. Kumari, B. S. Dwarakanath, A. Das, A. N. Bhatt, *Tumor Biol.* **2016**, *37*, 11553.
[8] T. Tanaka, M. Narazaki, T. Kishimoto, *Cold Spring Harb Perspect. Biol.* **2014**, *6*, a016295.
[9] T. Herold, V. Jurinovic, C. Arnreich, J. C. Hellmuth, M. von Bergwelt-Baildon, M. Klein, T. Weinberger, *medRxiv* **2020**, 2020.04.01.20047381.
[10] X. Chen, B. Zhao, Y. Qu, Y. Chen, J. Xiong, Y. Feng, D. Men, Q. Huang, Y. Liu, B. Yang, J. Ding, F. Li, *Clin. Infect. Dis.* **2020**, https://doi.org/10.1093/cid/ciaa449.
[11] F. Khosravi, S. M. Loeian, B. Panchapakesan, *Biosensors* **2017**, *7*, 17.
[12] M. Helle, L. Boeije, E. de Groot, A. de Vos, L. Aarden, *J. Immunol. Methods* **1991**, *138*, 47.
[13] J. Sabaté del Río, O. Y. F. Henry, P. Jolly, D. E. Ingber, *Nat. Nanotechnol.* **2019**, *14*, 1143.
[14] B. S. Munge, C. E. Krause, R. Malhotra, V. Patel, J. Silvio Gutkind, J. F. Rusling, *Electrochem. Commun.* **2009**, *11*, 1009.
[15] T. Li, M. Yang, *Sens. Actuators, B* **2011**, *158*, 361.
[16] R. Malhotra, V. Patel, J. P. Vaque, J. S. Gutkind, J. F. Rusling, J. P. Vaqué, J. S. Gutkind, J. F. Rusling, *Anal. Chem.* **2010**, *82*, 3118.
[17] M. A. Khan, M. Mujahid, *Sensors* **2020**, *20*, 646.
[18] G. Wang, H. Huang, B. Wang, X. Zhang, L. Wang, *Chem. Commun.* **2012**, *48*, 720.
[19] M. Tertiş, B. Ciui, M. Suciu, R. Săndulescu, C. Cristea, *Electrochim. Acta* **2017**, *258*, 1208.
[20] C. Diacci, M. Berto, M. Di Lauro, E. Bianchini, M. Pinti, D. Simon, F. Biscarini, C. A. Bortolotti, *Biointerphases* **2017**, *12*, 05F401.
[21] N. Liu, H. Yi, Y. Lin, H. Zheng, X. Zheng, D. Lin, H. Dai, *Microchim. Acta* **2018**, *185*, 277.
[22] X. P. Liu, X. L. Xie, Y. P. Wei, C. jie Mao, J. S. Chen, H. L. Niu, J. M. Song, B. K. Jin, *Microchim. Acta* **2018**, *185*, 52.
[23] T.-H. Chou, C.-Y. Chuang, C.-M. Wu, *Cytokine* **2010**, *51*, 107.
[24] J. F. Masson, *ACS Sens.* **2017**, *2*, 16.
[25] P. Chen, M. T. Chung, W. McHugh, R. Nidetz, Y. Li, J. Fu, T. T. Cornell, T. P. Shanley, K. Kurabayashi, *ACS Nano* **2015**, *9*, 4173.
[26] L. Luo, Z. Zhang, L. Hou, *Anal. Chim. Acta* **2007**, *584*, 106.
[27] L. Luo, Z. Zhang, L. Hou, J. Wang, W. Tian, *Talanta* **2007**, *72*, 1293.
[28] J. Wu, Y. Chen, M. Yang, Y. Wang, C. Zhang, M. Yang, J. Sun, M. Xie, X. Jiang, *Anal. Chim. Acta* **2017**, *982*, 138.
[29] J. Deng, M. Yang, J. Wu, W. Zhang, X. Jiang, *Anal. Chem.* **2018**, *90*, 9132.
[30] G. Liu, M. Qi, M. R. Hutchinson, G. Yang, E. M. Goldys, *Biosens. Bioelectron.* **2016**, *79*, 810.
[31] J. F. Djoba Siawaya, T. Roberts, C. Babb, G. Black, H. J. Golakai, K. Stanley, N. B. Bapela, E. Hoal, S. Parida, P. van Helden, G. Walzl, *PLoS One* **2008**, *3*, 2535.
[32] G. Liu, K. Zhang, A. Nadort, M. R. Hutchinson, E. M. Goldys, *ACS Sens.* **2017**, *2*, 218.
[33] X. Hun, Z. Zhang, *Biosens. Bioelectron.* **2007**, *22*, 2743.
[34] P. D'Orazio, *Clin. Chim. Acta* **2011**, *412*, 1749.
[35] T.-S. Wong, S. H. Kang, S. K. Y. Tang, E. J. Smythe, B. D. Hatton, A. Grinthal, J. Aizenberg, *Nature* **2011**, *477*, 443.
[36] M. Villegas, Y. Zhang, N. Abu Jarad, L. Soleymani, T. F. Didar, *ACS Nano* **2019**, *13*, 8517.
[37] M. Badv, S. M. Imani, J. I. Weitz, T. F. Didar, *ACS Nano* **2018**, *12*, 10890.
[38] A. Hosseini, M. Villegas, J. Yang, M. Badv, I. W. Jeffrey, L. Soleymani, F. T. Didar, *Adv. Mater. Interfaces* **2018**, *5*, 1800617.
[39] M. Badv, I. H. Jaffer, J. I. Weitz, T. F. Didar, *Sci. Rep.* **2017**, *7*, 11639.
[40] N. Vogel, R. A. Belisle, B. Hatton, T. S. Wong, J. Aizenberg, *Nat. Commun.* **2013**, *4*, 2167.
[41] D. C. Leslie, A. Waterhouse, J. B. Berthet, T. M. Valentin, A. L. Watters, A. Jain, P. Kim, B. D. Hatton, A. Nedder, K. Donovan, E. H. Super, C. Howell, C. P. Johnson, T. L. Vu, D. E. Bolgen, S. Rifai, A. R. Hansen, M. Aizenberg, M. Super, J. Aizenberg, D. E. Ingber, D. E. Ingber, *Nat. Biotechnol.* **2014**, *32*, 1134.
[42] J. Li, T. Kleintschek, A. Rieder, Y. Cheng, T. Baumbach, U. Obst, T. Schwartz, P. A. Levkin, *ACS Appl. Mater. Interfaces* **2013**, *5*, 6704.

[43] P. Wang, Z. Lu, D. Zhang, *Corros. Sci.* **2015**, *93*, 159.
[44] S. Yuan, S. Luan, S. Yan, H. Shi, J. Yin, *ACS Appl. Mater. Interfaces* **2015**, *7*, 19466.
[45] N. T. Darwish, S. D. Sekaran, Y. Alias, S. M. Khor, *J. Pharm. Biomed. Anal.* **2018**, *149*, 591.
[46] S. M. Imani, M. Badv, A. Shakeri, H. Yousefi, D. Yip, C. Fine, T. F. Didar, *Lab Chip* **2019**, *19*, 3228.
[47] P. Delfani, L. Dexlin Mellby, M. Nordström, A. Holmér, M. Ohlsson, C. A. K. Borrebaeck, C. Wingren, *PLoS One* **2016**, *11*, 0159138.
[48] S. Yatsushiro, R. Akamine, S. Yamamura, M. Hino, K. Kajimoto, K. Abe, H. Abe, J. Kido, M. Tanaka, Y. Shinohara, Y. Baba, T. Ooie, M. Kataoka, *PLoS One* **2011**, *6*, 18807.
[49] J. Foncy, A. Estève, A. Degache, C. Colin, J. C. Cau, L. Malaquin, C. Vieu, E. Trévisiol, in *Cell-Based Microarrays Methods Protoc.* (Eds: P. Ertl, M. Rothbauer), Springer New York, New York **2018**, pp. 83–95.
[50] R. Castagna, A. Bertucci, E. A. Prasetyanto, M. Monticelli, D. V. Conca, M. Massetti, P. P. Sharma, F. Damin, M. Chiari, L. De Cola, R. Bertacco, *Langmuir* **2016**, *32*, 3308.
[51] S. L. Seurynck-Servoss, A. M. White, C. L. Baird, K. D. Rodland, R. C. Zangar, *Anal. Biochem.* **2007**, *371*, 105.
[52] J. H. T. Luong, K. B. Male, J. D. Glennon, *Biotechnol. Adv.* **2008**, *26*, 492.
[53] L. Chen, P. Y. Qian, *Mar. Drugs* **2017**, *15*, 264.
[54] W. J. Yang, T. Cai, K. G. Neoh, E. T. Kang, S. L. M. Teo, D. Rittschof, *Biomacromolecules* **2013**, *14*, 2041.
[55] C. Rodriguez-Emmenegger, M. Houska, A. B. Alles, E. Brynda, *Macromol. Biosci.* **2012**, *12*, 1413.
[56] J. Jiang, L. Zhu, L. Zhu, H. Zhang, B. Zhu, Y. Xu, *ACS Appl. Mater. Interfaces* **2013**, *5*, 12895.
[57] S. Sathish, N. Ishizu, A. Q. Shen, *ACS Appl. Mater. Interfaces* **2019**, *11*, 46350.
[58] A. M. D. Wan, D. Devadas, E. W. K. Young, *Sens. Actuators, B* **2017**, *253*, 738.
[59] A. C. Glavan, R. V. Martinez, A. B. Subramaniam, H. J. Yoon, R. M. D. Nunes, H. Lange, M. M. Thuo, G. M. Whitesides, *Adv. Funct. Mater.* **2014**, *24*, 60.
[60] S. Oyola-Reynoso, I. D. Tevis, J. Chen, B. S. Chang, S. Çinar, J. F. Bloch, M. M. Thuo, *J. Mater. Chem. A* **2016**, *4*, 14729.
[61] V. V. Naik, R. Städler, N. D. Spencer, *Langmuir* **2014**, *30*, 14824.
[62] V. V. Naik, M. Crobu, N. V. Venkataraman, N. D. Spencer, *J. Phys. Chem. Lett.* **2013**, *4*, 2745.
[63] S. Oyola-Reynoso, Z. Wang, J. Chen, S. çinar, B. Chang, M. Thuo, *Coatings* **2015**, *5*, 1002.
[64] P. Samyn, *J. Mater. Sci.* **2013**, *48*, 6455.
[65] G. Beamson, D. Briggs, *J. Chem. Educ.* **1993**, *70*, A25.
[66] S. Pletincx, K. Marcoen, L. Trotochaud, L. L. Fockaert, J. M. C. Mol, A. R. Head, O. Karslioğlu, H. Bluhm, H. Terryn, T. Hauffman, *Sci. Rep.* **2017**, *7*, 13341.
[67] V. Dugas, Y. Chevalier, *J. Colloid Interface Sci.* **2003**, *264*, 354.
[68] A. Shakeri, S. Rahmani, S. M. Imani, M. Osborne, H. Yousefi, T. F. Didar, in *Bioelectron. Med. Devices from Mater. to Devices - Fabr. Appl. Reliab.* (Eds: K. Pal, H.-B. Kraatz, A. Khasnobish, S. Bag, I. Banerjee, U. Kuruganti), Woodhead Publishing, Cambridge, Massachusetts **2019**, pp. 635–699.
[69] X. Cui, Y. Gao, S. Zhong, Z. Zheng, Y. Cheng, H. Wang, *J. Polym. Res.* **2012**, *19*, 9832.
[70] T. Song, Q. Liu, J. Liu, W. Yang, R. Chen, X. Jing, K. Takahashi, J. Wang, *Appl. Surf. Sci.* **2015**, *355*, 495.
[71] C. S. Park, E. Y. Jung, H. J. Jang, G. T. Bae, B. J. Shin, H. S. Tae, *Polymers* **2019**, *11*, 396.
[72] H. R. Tantawy, B. A. F. Kengne, D. N. McIlroy, T. Nguyen, D. Heo, Y. Qiang, D. E. Aston, *J. Appl. Phys.* **2015**, *118*, 175501.
[73] L. Zhang, Y. Li, L. Zhang, D. W. Li, D. Karpuzov, Y. T. Long, *Int. J. Electrochem. Sci.* **2011**, *6*, 819.
[74] A. Shukla, S. D. Bhat, V. K. Pillai, *J. Membr. Sci.* **2016**, *520*, 657.
[75] G. Panomsuwan, N. Saito, T. Ishizaki, *J. Mater. Chem. A* **2015**, *3*, 9972.
[76] A. R. Barron, *Physical Methods in Chemistry and Nano Science*, Rice University, Houston, TX **2012**.
[77] M. Badv, J. I. Weitz, T. F. Didar, *Small* **2019**, *15*, 1905562.
[78] M. Badv, C. Alonso-Cantu, A. Shakeri, Z. Hosseinidoust, J. I. Weitz, T. F. Didar, *ACS Biomater. Sci. Eng.* **2019**, *5*, 6485.
[79] J. Schindelin, I. Arganda-Carreras, E. Frise, V. Kaynig, M. Longair, T. Pietzsch, S. Preibisch, C. Rueden, S. Saalfeld, B. Schmid, J.-Y. Tinevez, D. J. White, V. Hartenstein, K. Eliceiri, P. Tomancak, A. Cardona, *Nat. Methods* **2012**, *9*, 676.
[80] P. Getreuer, *Image Process. Line* **2012**, *2*, 214.
[81] S. Van Der Walt, J. L. Schönberger, J. Nunez-Iglesias, F. Boulogne, J. D. Warner, N. Yager, E. Gouillart, T. Yu, *PeerJ* **2014**, *2*, 453.
[82] L. Fayad, M. J. Keating, J. M. Reuben, S. O'Brien, B. N. Lee, S. Lerner, R. Kurzrock, *Blood* **2001**, *97*, 256.
[83] H. Knüpfer, R. Preiß, *Breast Cancer Res. Treat.* **2007**, *102*, 129.
[84] J. Nakashima, M. Tachibana, Y. Horiguchi, M. Oya, T. Ohigashi, H. Asakura, M. Murai, *Clin. Cancer Res.* **2000**, *6*, 2702 LP.
[85] D. J. George, S. Halabi, T. F. Shepard, B. Sanford, N. J. Vogelzang, E. J. Small, P. W. Kantoff, *Clin. Cancer Res.* **2005**, *11*, 1815.
[86] M. Plante, S. C. Rubin, G. Y. Wong, M. G. Federici, C. L. Finstad, G. A. Gastl, *Cancer* **1994**, *73*, 1882.
[87] J. Kim, A. S. Campbell, B. E.-F. de Ávila, J. Wang, *Nat. Biotechnol.* **2019**, *37*, 389.